

## Numerical simulations of optical properties of Saharan dust aerosols with emphasis on lidar applications

M. Wiegner, J. Gasteiger, K. Kandler, B. Weinzierl, K. Rasp, M. Esselborn, V. Freudenthaler, B. Heese, C. Toledano, M. Tesche & D. Althausen

To cite this article: M. Wiegner, J. Gasteiger, K. Kandler, B. Weinzierl, K. Rasp, M. Esselborn, V. Freudenthaler, B. Heese, C. Toledano, M. Tesche & D. Althausen (2009) Numerical simulations of optical properties of Saharan dust aerosols with emphasis on lidar applications, *Tellus B: Chemical and Physical Meteorology*, 61:1, 180-194, DOI: [10.1111/j.1600-0889.2008.00381.x](https://doi.org/10.1111/j.1600-0889.2008.00381.x)

To link to this article: <https://doi.org/10.1111/j.1600-0889.2008.00381.x>



© 2009 The Author(s). Published by Taylor & Francis.



Published online: 18 Jan 2017.



Submit your article to this journal [↗](#)



Article views: 9



View related articles [↗](#)



Citing articles: 6 View citing articles [↗](#)

# Numerical simulations of optical properties of Saharan dust aerosols with emphasis on lidar applications

By M. WIEGNER<sup>1\*</sup>, J. GASTEIGER<sup>1</sup>, K. KANDLER<sup>2</sup>, B. WEINZIERL<sup>3</sup>, K. RASP<sup>3</sup>,  
M. ESSELBORN<sup>3</sup>, V. FREUDENTHALER<sup>1</sup>, B. HEESE<sup>1,4</sup>, C. TOLEDANO<sup>1</sup>, M. TESCHE<sup>4</sup>  
and D. ALTHAUSEN<sup>4</sup>, <sup>1</sup>Ludwig-Maximilians-Universität, Meteorologisches Institut, Theresienstrasse 37,  
80333 München, Germany; <sup>2</sup>Institute for Applied Geosciences, Darmstadt University of Technology, Darmstadt,  
Germany; <sup>3</sup>Deutsches Zentrum für Luft- und Raumfahrt (DLR), Institut für Physik der Atmosphäre, Oberpfaffenhofen,  
82234 Wessling, Germany; <sup>4</sup>Institute for Tropospheric Research (IfT), Leipzig, Germany

(Manuscript received 19 December 2007; in final form 1 August 2008)

## ABSTRACT

In the framework of the Saharan Mineral Dust Experiment (SAMUM) for the first time the spectral dependence of particle linear depolarization ratios was measured by combining four lidar systems. In this paper these measurements are compared with results from scattering theory based on the T-matrix method. For this purpose, in situ measurements—size distribution, shape distribution and refractive index—were used as input parameters; particle shape was approximated by spheroids. A sensitivity study showed that lidar-related parameters—lidar ratio  $S_p$  and linear depolarization ratio  $\delta_p$ —are very sensitive to changes of all parameters. The simulated values of the  $\delta_p$  are in the range of 20% and 31% and thus in the range of the measurements. The spectral dependence is weak, so that it could not be resolved by the measurements. Calculated lidar ratios based on the measured microphysics and considering equivalent radii up to 7.5  $\mu\text{m}$  show a range of possible values between 29 and 50 sr at  $\lambda = 532\text{ nm}$ . Larger  $S_p$  might be possible if the real part of the refractive index is small and the imaginary part is large. A strict validation was however not possible as too many microphysical parameters influence  $S_p$  and  $\delta_p$  that could not be measured with the required accuracy.

## 1. Introduction

The fourth assessment of the IPCC again emphasized that aerosol particles, including mineral dust, are one of the main gaps in our present knowledge of the radiative forcing (Solomon et al., 2007). A major issue is the fact that mineral particles cannot be considered as spherical and thus, ‘conventional’ scattering theories such as the Mie theory cannot be applied. As a consequence, an improvement of predictions of future climate requires increasing efforts to understand and model the effects of this aerosol component, in particular, as its abundance is significant and the distribution almost global. Furthermore, the consideration of the non-sphericity of mineral dust is important for remote sensing applications, for example, the inversion of satellite data, lidar or sun photometer measurements (Nicolae et al., 2004; Veihelmann et al., 2004; Dubovik et al., 2006; Yang et al., 2007).

To investigate the characteristics of mineral dust near its major source region, the Saharan desert, the field campaign ‘Saharan Mineral Dust Experiment’ (SAMUM) was proposed and performed between 13 May and 7 June 2006 in Ouarzazate and Tinfou, Morocco.

Saharan Mineral Dust Experiment offered an excellent opportunity to investigate the radiative properties of mineral dust. On the one hand, comprehensive measurements of microphysical properties at ground and different altitudes in the dust layer were made. These include particle size distribution, chemical composition and geometrical shape, and the refractive index as a function of wavelength. On the other hand, up to four lidar systems were operated simultaneously, providing profiles of extinction and backscatter coefficients of the particles at several wavelengths. For the first time, linear depolarization ratios at the wavelengths of 355, 532, 710 and 1064 nm were measured with the lidars. This unique data set offers the chance to calculate optical properties on the basis of realistic input data, and the opportunity to compare the model results with independent measurements.

In this paper, we focus on optical properties of mineral dust particles calculated on the basis of microphysical data measured

\*Corresponding author.

e-mail: m.wiegner@lmu.de

DOI: 10.1111/j.1600-0889.2008.00381.x

during the SAMUM campaign. In the following section, we outline the model (T-matrix) and the inherent assumptions. Then, we describe the microphysical properties of the particles that we used to initialize the model. In Section 4, we discuss the main results, in particular those quantities that are relevant for lidar remote sensing. Additionally, we investigate the influence of changes in the microphysical properties on the optical properties of the particles to estimate the consequences of possible uncertainties of the measurement and the natural variability of the dust layers. Finally, our findings are compared to measurements and summarized.

## 2. Modelling of optical properties

Optical properties of mineral aerosol particles cannot be determined from Mie theory, as the particles are non-spherical. Candidates for an adequate numerical treatment are the T-matrix method (Waterman, 1971), the discrete dipole approximation (Purcell and Pennypacker, 1973), geometrical optics approach (GOA; Macke and Mishchenko, 1996; Yang and Liou, 1996) or the finite difference time domain method (Yee, 1966). The choice of the most suitable method depends on several issues: First, it is important whether the particles must be approximated by an idealized shape (which is, e.g. rotational symmetric) or if they can be completely irregular. Second, the size of the particles is crucial as the applicability of most models is limited to a certain size range. And finally, the required computer time must be considered, in particular because a series of sensitivity studies is required to investigate the influence of different microphysical parameters on the optical properties.

In this study, we assume that the particles can be approximated by spheroids. This approach is necessary since only rotationally symmetric shapes can be handled by current numerical tools in the size range required for this study. Optical properties of cylinders are also presented in this paper for comparison. Figure 1 shows two particles collected during SAMUM, and the corresponding approximation of its shape by a spheroid (in two dimensions shown as ellipse). Though the general shape of both particles is well approximated by the ellipses, it is obvious, that nevertheless sharp edges and small-scaled structures are present in natural dust particles.

Spheroids are ellipses rotated around one axis; if this axis is the longer axis, they are called prolate, otherwise oblate. The geometry of these particles is defined by two parameters: one parameter for the shape and one for the size. As shape parameter the ratio  $\varepsilon$  of the lengths of the axis perpendicular to the rotational axis and the rotational axis is used. As a consequence,  $\varepsilon$  is smaller than 1 for prolate spheroids and vice versa for oblate spheroids. Additionally, the aspect ratio  $\varepsilon'$  is defined. The aspect ratio is the ratio of the largest to the smallest particle dimension, that is, always larger than or equal to 1. Hence for oblate spheroids the aspect ratio  $\varepsilon'$  is equal to  $\varepsilon$ , for prolate spheroids it is  $\varepsilon^{-1}$ . Spheroids with  $\varepsilon' = 1$  are obviously spheres. The aspect ratio

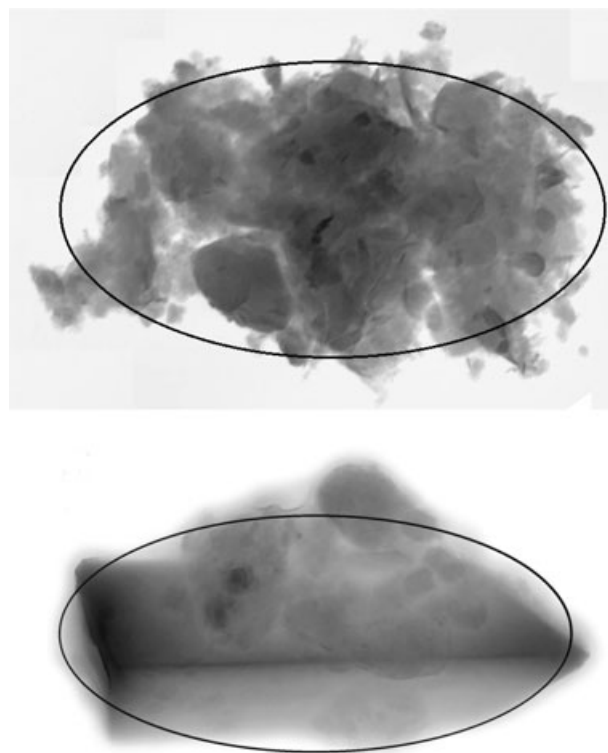


Fig. 1. Electron micrographs of non-spherical particles and their approximations by spheroids/ellipses (longer axis are  $6.3 \mu\text{m}$  (upper figure) and  $11.6 \mu\text{m}$ ).

can be used as a measure for the deviation of a particle from the spherical shape. In this paper, the size of a particle is described by the radius  $r$  of a sphere with the same surface.

For spheroids the T-matrix method is a suitable numerical tool, in particular, as it is an exact method based on a solution of Maxwell's equations. It can also be applied to cylinders and Chebyshev particles. A respective FORTRAN code is provided by Mishchenko and Travis (1998). The code is available in two versions, a 'double precision' and an 'extended precision' version. The latter is more time consuming, but allows the application to larger size parameters  $x = 2\pi r/\lambda$  ( $r$  as defined above), so that it is used here. The required computer time on a standard workstation for three different aspect ratios  $\varepsilon'$  as a function of the size parameter  $x$  is shown in Fig. 2. Figure 2 also shows the range of applicability for different pairs of  $x$  and  $\varepsilon'$ ; for  $m$  we select a typical value for  $\lambda = 532 \text{ nm}$ .

It can be seen that large aspect ratios and large size parameters significantly increase the required computer time. As the size parameter approaches  $x = 100$ , the calculation time for a single particle is more than 1 h. It is also obvious that the larger  $\varepsilon'$  the smaller is the maximum  $x$  where numerical convergence can be obtained (see below). Convergence is controlled by the parameter DDELT. It is usually set to  $10^{-6}$  to increase the numerical stability at the expense of a slightly increased computation time. Only for large particles, the recommended value

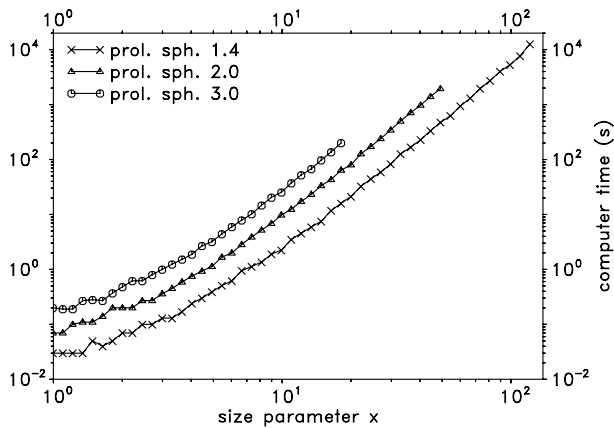


Fig. 2. Required computer time as a function of size parameter for prolate spheroids with different aspect ratios; refr. index  $m = 1.56 + 0.0043i$ , DDELT =  $10^{-6}$ , Intel Xeon 5130 processor, one thread.

(DDELT =  $10^{-3}$ ) given in Mishchenko and Travis (1998) is applied. Because of the limited size parameter range, the application of the GOA seems to be useful for large particles. However, as we focus on lidar applications, the inaccuracy of this approach for the scattering angle of  $180^\circ$  (see e.g. Wielgaard et al., 1997) prevents us from using it in this paper. Nevertheless, a brief comment is given at the end of Section 4.1.

For our simulations we have established a database of optical properties for individual spheroidal particles. We have performed calculations for size parameters from  $x = 0.001$  up to the limit of convergence, which never exceeds  $x = 135$ , for logarithmic intervals: each particle is 3% larger than the previous, that is,  $x_{i+1} = 1.03x_i$ . The aspect ratio is varied between  $\varepsilon' = 1.2$  and  $\varepsilon' = 3.0$  in intervals of  $\Delta\varepsilon' = 0.2$ . Oblate and prolate spheroids are considered. Refractive indices  $m$  are taken from measurements (see below). The database includes the Mueller matrix  $\mathbf{P}(\psi)$ — $\psi$  being the scattering angle—and extinction and scattering cross-sections ( $C_e$ ,  $C_s$ ). These parameters constitute the complete basis for radiative transfer calculations and remote sensing studies. In this paper, however, only  $P_{11}(\psi)$ , that is, the phase function, and  $P_{22}(\psi)$ , are relevant elements of the Mueller matrix.

Having the optical properties of single particles, the optical properties of any size distribution and/or shape distribution can easily be derived from weighted means. The corresponding equations can be found in many standard text books.

In this paper, we explicitly discuss the extinction coefficient  $\beta_e$ , the Ångström coefficient  $\alpha$ , the single scattering albedo  $\omega_0$  and the asymmetry parameter  $g$ . Furthermore, the lidar ratio  $S_p$  and the linear depolarization ratio  $\delta_p$ , are derived for lidar applications. For convenience, we have listed the definitions of these parameters below.

$$\beta_e = \int_0^{r_{\max}} C_e(r) \frac{dN(r)}{dr} dr,$$

$$\alpha = \frac{\ln(\beta_e(\lambda_1)/\beta_e(\lambda_2))}{\ln(\lambda_2/\lambda_1)},$$

$$\omega_0 = C_s/C_e,$$

$$g = \frac{1}{2} \int_{-1}^1 P_{11}(\psi) \cos \psi d(\cos \psi),$$

$$S_p = \frac{4\pi}{\omega_0 P_{11}(180^\circ)},$$

$$\delta_p = \frac{P_{22}(180^\circ) - P_{11}(180^\circ)}{P_{22}(180^\circ) + P_{11}(180^\circ)}.$$

Here,  $dN/dr$  is the number density of the particles per radius interval, and  $r$  the equivalent radius of the particles.

We select wavelengths  $\lambda$  that correspond to the lidar systems that have been operated during SAMUM. They include POLIS (providing  $\delta_p$  at  $\lambda = 355$  nm), MULIS (providing  $\delta_p$  at  $\lambda = 532$  nm), both systems of the University of Munich, BERTHA (providing  $\delta_p$  at  $\lambda = 710$  nm) of the IfT Leipzig and the high spectral resolution lidar HSRL (providing  $\delta_p$  at  $\lambda = 532$  and  $\lambda = 1064$  nm) of the DLR. Lidar ratios can be derived from lidars working in either the Raman mode (MIM, IfT) or HSRL mode (DLR).

### 3. Microphysical parameters

To calculate optical parameters with the method described in the previous section, input from SAMUM measurements is required: it includes information about particle size, particle shape and refractive index. As will be discussed later, the shape distribution and the refractive index depend on the size of the particles. Note, that we also have to consider limitations of the T-matrix approach with respect to the maximum  $x$ .

First, we define a ‘reference case’ as the basis for sensitivity studies. As reference case we selected a situation when the aerosol layer has been very homogeneous and stable in time. Such conditions are found for 19 May 2006, as measurements over and at Ouarzazate demonstrate. On this day the aerosol layer extends up to 5 km above sea level. The homogeneity is verified by in situ measurements and confirmed by vertical extinction coefficient profiles derived from the lidars. This reference case is described by an averaged size distribution, shape distribution and wavelength-dependent refractive index.

We approximate the particles by spheroids having random orientation. To account for the large variety of natural mineral dust particle shapes a wide aspect ratio distribution is applied. Mishchenko et al. (1997) found, that by averaging the optical properties over a wide range of aspect ratios, the agreement with measured phase functions of mineral dust is remarkably better compared to the case, when only one spheroidal shape is used. This finding was confirmed by Nousiainen and Vermeulen (2003). Shape distributions, providing the relative number of particles of a given aspect ratio, are available from literature (e.g. Mishchenko et al., 1997; Dubovik et al., 2006), however,

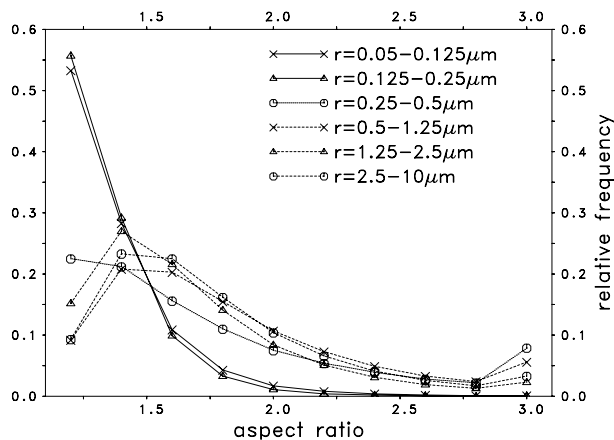


Fig. 3. Aspect ratio distributions derived from electron microscopy for size intervals as indicated; for details see Kandler et al. (2008).

for the reference case we prefer—for reasons of consistency—distributions from measurements of Kandler during SAMUM (2008, this issue). They are derived from electron-microscopical single particle analysis of ground-based samples and from airborne samples that were collected in 1.5 and 4.85 km height above sea level from the Partenavia and Falcon platforms, respectively. As the distributions in the different heights are almost identical, the samples can be considered representative for the whole aerosol layer. For the reference case we use only prolate spheroids. This choice is supported by findings of Nousiainen and Vermeulen (2003). They have shown that simulations with prolate spheroids are in better agreement with measured scattering matrix elements of mineral dust particles, than those of oblate or a equiprobable mixture of prolate and oblate spheroids.

The relative frequency of particles with a given aspect ratio, henceforward referred to as shape distribution, is shown in Fig. 3. It shows several shape distributions for different size intervals, for example,  $0.05 \leq r \leq 0.125 \mu\text{m}$  and  $0.125 \leq r \leq 0.25 \mu\text{m}$ , revealing a significant dependence on the particle size. In case of particles  $r < 0.25 \mu\text{m}$ , both aspect ratio distributions (full lines in Fig. 3) are quite similar and show a decrease with increasing aspect ratio. For particles with  $r > 0.5 \mu\text{m}$  all shape distributions also do not differ significantly from each other having a small maximum at  $\varepsilon' = 1.4$  and  $\varepsilon' = 1.6$ . However, they are quite different from the distribution of small particles. The distribution for particles between  $r = 0.25$  and  $r = 0.5 \mu\text{m}$  is the transition between the two regimes. According to these measurements we define two different shape distributions for our reference case: one applicable to particles with  $r < 0.35 \mu\text{m}$  and one for larger particles. These distributions are averages over the corresponding range-resolved measurements as shown in Fig. 3 and given in Table 1. The median aspect ratio is near 1.3 for the small particles, while it is about 1.65 for the larger ones.

As the shape distribution is size-dependent it is obvious that the choice of a size distribution influences the relative frequency of particle shapes. For example, in a size distribution with a very

Table 1. Aspect ratio distribution of the reference case: the first line represents a range from  $\varepsilon' = 1.0$  to  $\varepsilon' = 1.3$ , the last line is for  $\varepsilon' > 2.9$ . All other values cover an  $\varepsilon'$ -intervall of 0.2

| $\varepsilon'$ | $r < 0.35 \mu\text{m}$ | $r > 0.35 \mu\text{m}$ |
|----------------|------------------------|------------------------|
| 1.2            | 0.535                  | 0.103                  |
| 1.4            | 0.289                  | 0.234                  |
| 1.6            | 0.108                  | 0.218                  |
| 1.8            | 0.040                  | 0.157                  |
| 2.0            | 0.015                  | 0.101                  |
| 2.2            | 0.007                  | 0.065                  |
| 2.4            | 0.003                  | 0.041                  |
| 2.6            | 0.001                  | 0.027                  |
| 2.8            | 0.001                  | 0.018                  |
| 3.0            | 0.001                  | 0.036                  |

high number of small particles, low aspect ratios of 1.2 and 1.4 will be more frequent.

To determine particle size distributions, a set of instruments containing several condensation particle counters (CPC) and optical spectrometers (PCASP-100X, FSSP-300, FSSP-100, Grimm OPC) was operated on the Falcon aircraft. More details on the in situ size distribution measurements and their parametrization by four-modal log-normal distributions are given by Weinzierl et al. (2008). The fit reads:

$$\frac{dN}{dr} = \sum_{i=1}^4 \frac{1}{\sqrt{2\pi}} \frac{N_{0,i}}{\ln \sigma_i} \frac{1}{r} \exp\left(-\left(\frac{\ln r - \ln r_{0,i}}{\sqrt{2} \ln \sigma_i}\right)^2\right).$$

$N_{0,i}$  (number density),  $\sigma_i$  (width) and  $r_{0,i}$  (modal radius) are the parameters for mode  $i$  of the log-normal distribution.  $N_{0,i}$  are normalized to standard conditions (273 K, 1013 hPa). Similar to the shape distributions, the size distributions do not show significant differences with height on 19 May 2006, so that one size distribution, that is, the average of the distributions found in 3.25 km (Level 3; 11:44 UT–12:06 UT) and 4.85 km (Level 2; 11:23 UT–11:37 UT), is used for the reference case. The parameters for the reference case are listed in Table 2.

By heating the aerosols to 250 °C, volatile aerosol components were identified, mainly on particles with  $r \leq 0.25 \mu\text{m}$ . These volatile aerosol components are present as a coating on a non-volatile core. In our simulations the first mode of the four-modal log-normal distribution represents this coated fraction.

Table 2. Size distribution of the reference case

| Mode $i$ | $N_{0,i}$ ( $\text{cm}^{-3}$ ) | $r_{0,i}$ ( $\mu\text{m}$ ) | $\sigma_i$ |
|----------|--------------------------------|-----------------------------|------------|
| 1        | 785                            | 0.039                       | 2.2        |
| 2        | 20                             | 0.2475                      | 1.7        |
| 3        | 9.65                           | 0.70                        | 1.9        |
| 4        | 0.64                           | 3.25                        | 1.7        |

According to the ammonium sulphate coating, we assume these particles as non-absorbing. Modes 2–4 represent the non-volatile mineral components (for details of the particle analyses see Kandler et al., 2008, Petzold et al., 2008, Weinzierl et al., 2008; this issue).

The refractive index of the particles is wavelength-dependent. To obtain the refractive index, measurements of the dust absorption coefficient were conducted at three wavelengths (from 467 to 660 nm) by means of a Particle Soot Absorption Photometer (PSAP; Virkkula et al., 2005) onboard the Falcon. Fiebig (2001) showed that the radius at which 50% of the particles pass the isokinetic inlet and enter the PSAP instrument is approximately  $1.25 \mu\text{m}$  at ground level and decreases to  $0.75 \mu\text{m}$  at an altitude of 10 km. However, Kandler et al., (2008, this issue) shows, that particles above and below  $r = 1.25 \mu\text{m}$  should have similar complex refractive indices. The analysis of the PSAP data is subject of a paper by Petzold et al., (2008, this issue), so the derivation of the refractive indices is only briefly outlined in the following.

First, a realistic chemical composition of the particles is assumed. The selected key components dominating dust optical properties follow the proposal of Sokolik and Toon (1999) and the spectral refractive indices of the individual chemical constituents are taken from the literature (Arakawa et al., 1997; Sokolik and Toon, 1999). The aerosol is assumed to consist of one merely scattering component like quartz or ammonium sulphate, one light absorbing component with a weak spectral dependence of the absorption coefficient as black carbon or kaolinite, and one light absorbing component with a strong spectral dependence of the absorption coefficient as haematite. The real and imaginary part of the refractive index is calculated as a linear combination of the refractive indices of the individual components weighted by their volume fraction. In a second step, a combined size distribution covering the range of the PSAP is calculated from CPC and PCASP-100X data. The size distribution and the refractive index serve as input data for a Mie model that computes the PSAP response. If the measured and calculated PSAP response at 467, 530 and 660 nm do not agree, the chemical composition is slightly varied until the inverted PSAP signal matches the measured PSAP signal within 3%. An overview of the refractive indices used for the reference case is given in Table 3.

With these parameters the calculation of optical properties can be performed. The only remaining problem is that for large

Table 3. Refractive indices for different modes of the size distribution (reference case)

| Wavelength (nm) | Mode 1        | Modes 2–4          |
|-----------------|---------------|--------------------|
| 355             | $1.5400 + 0i$ | $1.580 + 0.0078i$  |
| 532             | $1.5305 + 0i$ | $1.560 + 0.0043i$  |
| 710             | $1.5200 + 0i$ | $1.554 + 0.0022i$  |
| 1064            | $1.5100 + 0i$ | $1.548 + 0.00195i$ |

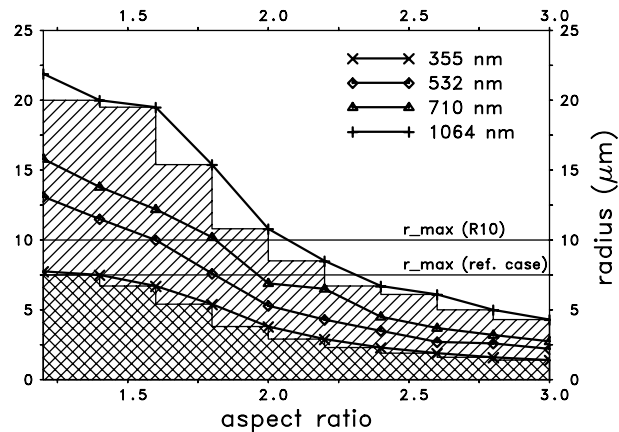


Fig. 4. Maximum radius  $r_{\text{max}}$  for the application of the T-matrix method; given for spheroids with given aspect ratios, wavelength as indicated.

particles with large aspect ratios the T-matrix method does not converge (confer Fig. 2). As the critical parameter is the size parameter  $x$ , one gets for each wavelength different maximum particle radius  $r_{\text{max}}$  up to which T-matrix calculations are possible. These limits are shape-dependent. An overview is given in Fig. 4. The solid lines indicate  $r_{\text{max}}$  of specific aspect ratios; the respective wavelengths are given in the figure. The double-hatched area bounded by the stepwise line indicates the spheroid spectrum, where T-matrix calculations are possible for all wavelengths considering the discrete grid of aspect ratios covered by our database. The upper limit is  $r_{\text{max}} = 7.5 \mu\text{m}$ . The influence of  $r_{\text{max}}$  on the optical properties is discussed later.

It is obvious from Fig. 4 that, for example, particles of  $r = 5 \mu\text{m}$  and  $\epsilon' = 1.4$  can be treated by the T-matrix method for all four wavelengths, but particles of  $r = 5 \mu\text{m}$  and  $\epsilon' = 2.6$  can only be modelled if the wavelength is 1064 nm. As we wanted the reference case to comprise the same particle spectrum for all wavelengths—only this approach guarantees a consistent derivation of the spectral behaviour of the optical properties—we have to consider the ‘worst’ case, that is, we have to define a shape distribution that can be handled for the shortest wavelength (355 nm). This idea will, however, not allow to consider all particles up to  $7.5 \mu\text{m}$  as suggested by the shape distribution measurements. Therefore, we substitute large particles if they do not fall into the common range of application of the T-matrix method (double-hatched area), by particles of the same size but the largest possible aspect ratio. For example, the above mentioned particles of  $r = 5 \mu\text{m}$  and  $\epsilon' = 2.6$  are substituted by a particle of  $r = 5 \mu\text{m}$  and  $\epsilon' = 1.8$ . The same is true for particles of  $r = 5 \mu\text{m}$  and  $\epsilon' = 2.8$  and so on. In the end all particles of  $r = 5 \mu\text{m}$  and  $\epsilon' \geq 1.8$  are modelled with  $\epsilon' = 1.8$ . Though this strategy requires some adaptations of the original data, these modifications are tolerated to ensure an exact model of the wavelength dependence of optical properties.

Alternatively, we choose the following ‘wavelength-dependent’ approach: for each wavelength and each particle radius we consider all  $\varepsilon'$  that fall into the range of application of the T-matrix method (see Fig. 4) for the given wavelength. The consequence of this procedure is that we do not have the same particle ensembles for all wavelengths, but we have used the results from the T-matrix calculations in the most extensive way. For example, if we consider  $\lambda = 1064$  nm (see hatched area), the full range of  $\varepsilon'$  from 1.2 to 3.0 can be applied to all particles smaller than  $4.3 \mu\text{m}$ . For particles as large as  $r = 7.5 \mu\text{m}$ ,  $\varepsilon' \leq 2.2$  can be considered. It is clear that for  $\lambda = 355$  nm the alternative approach gives the same results as the procedure described first.

## 4. Results

In this section we discuss the results of our numerical simulations with special emphasis on the influence of different microphysical properties on the optical properties of the aerosol ensemble. To make the results comparable, we confine the results to simulations that consider particles not larger than  $r = 7.5 \mu\text{m}$ . The effect of larger particles might be relevant when simulations are compared to retrievals of remote sensing techniques, and consequently discussed mainly in Section 5.

### 4.1. Reference case

First we refer to the primary information that describes all optical properties depending on the scattering angle  $\psi$ , the Mueller matrix  $\mathbf{P}(\psi)$ . The element  $P_{11}(\psi)$  allows to determine the asymmetry parameter  $g$  and the lidar ratio  $S_p$ . From  $P_{22}(\psi)$  and  $P_{11}(\psi)$  the linear depolarization ratio  $\delta_p$  can be derived. These elements as a function of  $\psi$  for  $\lambda = 532$  nm are shown in Fig. 5: the reference case (particles being prolate spheroids) and, for comparison, the results for spheres derived from Mie theory.

The comparison between the reference case and spheres shows the well-known fact that the assumption of spherical particles significantly influences the phase function. While  $P_{11}(\psi)$  is nearly constant for  $100^\circ < \psi < 150^\circ$  in the reference case, for spherical particles  $P_{11}(\psi)$  has a pronounced minimum near  $125^\circ$ . The differences between both phase functions can be larger than a factor of two for scattering angles  $\psi > 100^\circ$ . In particular,  $P_{11}$  in backward direction ( $\psi = 180^\circ$ ), relevant for the lidar ratio, shows a pronounced difference.  $P_{22}(\psi)/P_{11}(\psi)$  is 1 for spherical particles, but smaller than 1 for non-spherical particles; it can be used for the discrimination between spherical and non-spherical particles.

The most important optical properties that do not depend on the scattering angle are summarized in Table 4 for the reference case (label ‘REF’), and—for comparison—for spheres (label ‘S’). The last two columns are explained later. Values are given for the four wavelengths of the lidars. As these wavelengths cover the range from the UV to the near infrared, they can also be used for studies of the radiation budget or remote sensing in this most relevant spectral region of solar radiation.

The extinction coefficient slightly decreases with wavelength, resulting in an Ångström coefficient of  $\alpha = 0.032$ , when the wavelength interval from 355 to 1064 nm is considered. In case of surface-equivalent spheres, the absolute values of the extinction coefficient are almost the same: the relative differences are in the order of 0.3%, and thus negligible. As a consequence, the Ångström coefficient does not differ from the non-spherical reference case. If the wavelength range is split into two intervals, that is, 355–532 nm and 532–1064 nm, it is found that  $\alpha$  is wavelength-dependent: for example, for the REF case it is 0.021 and 0.039, respectively.

The single scattering albedo  $\omega_0$  increases with wavelength from  $\omega_0 = 0.75$  to  $\omega_0 = 0.95$ . That means that absorption is strongest at the shorter wavelengths as expected from the imaginary part of the refractive index (see Table 3). The difference

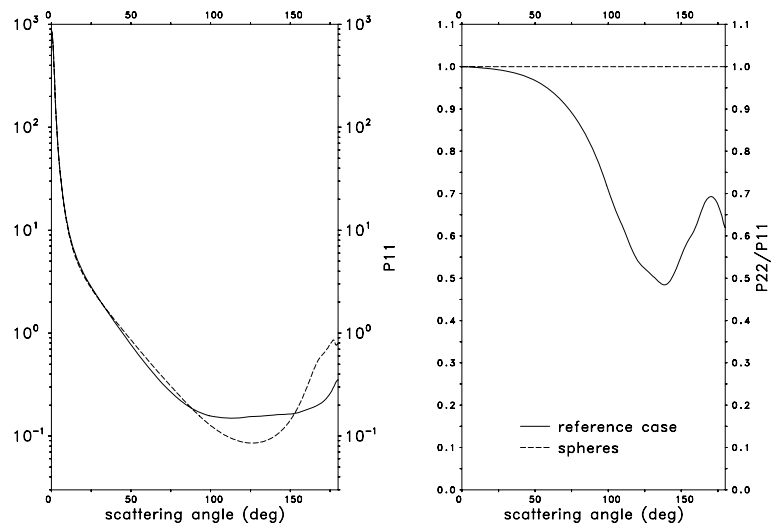


Fig. 5. Elements  $P_{11}(\psi)$  and  $P_{22}(\psi)/P_{11}(\psi)$  of the Mueller matrix;  $\lambda = 532$  nm: reference case with T-Matrix (full line), Mie theory (dashed line).

Table 4. Optical properties of the reference case (REF), spherical particles (S), an alternative approach for spheroids (ALT) and consideration of larger particles (R10); for details, see text

| Parameter                         | $\lambda$ (nm) | S      | REF    | ALT    | R10    |
|-----------------------------------|----------------|--------|--------|--------|--------|
| $\beta_e$<br>( $\text{km}^{-1}$ ) | 355            | 0.1760 | 0.1757 | 0.1757 | 0.1883 |
|                                   | 532            | 0.1739 | 0.1742 | 0.1742 | 0.1870 |
|                                   | 710            | 0.1721 | 0.1720 | 0.1721 | 0.1849 |
|                                   | 1064           | 0.1701 | 0.1696 | 0.1696 | 0.1827 |
| $\alpha$                          | 355–1064       | 0.031  | 0.032  | 0.032  | 0.027  |
| $\omega_0$                        | 355            | 0.7482 | 0.7496 | 0.7496 | 0.7366 |
|                                   | 532            | 0.8444 | 0.8440 | 0.8447 | 0.8303 |
|                                   | 710            | 0.9205 | 0.9191 | 0.9197 | 0.9097 |
|                                   | 1064           | 0.9458 | 0.9450 | 0.9455 | 0.9383 |
| $g$                               | 355            | 0.7975 | 0.7976 | 0.7976 | 0.8048 |
|                                   | 532            | 0.7642 | 0.7622 | 0.7630 | 0.7707 |
|                                   | 710            | 0.7361 | 0.7285 | 0.7311 | 0.7379 |
|                                   | 1064           | 0.7140 | 0.7083 | 0.7120 | 0.7185 |
| $S_p$<br>(sr)                     | 355            | 26.6   | 59.7   | 59.7   | 63.4   |
|                                   | 532            | 18.9   | 42.4   | 42.5   | 45.0   |
|                                   | 710            | 13.9   | 30.8   | 31.1   | 32.2   |
|                                   | 1064           | 12.5   | 28.5   | 28.9   | 29.5   |
| $\delta_p$                        | 355            | 0      | 0.2072 | 0.2072 | 0.2051 |
|                                   | 532            | 0      | 0.2348 | 0.2353 | 0.2332 |
|                                   | 710            | 0      | 0.2432 | 0.2451 | 0.2403 |
|                                   | 1064           | 0      | 0.2650 | 0.2677 | 0.2618 |

between the spherical and non-spherical case is again negligible. The asymmetry parameter  $g$  (i.e. the expectation value of the cosine of the scattering angle) is determined from the phase function  $P_{11}(\psi)$  (see Fig. 5, left-hand panel) and is slightly decreasing with  $\lambda$  in accordance with the less pronounced forward scattering in the near infrared. The differences between spherical and non-spherical particle ensembles can reach 0.8%, that means, they are still small, but larger than the differences in the extinction or the single scattering albedo.

The lidar-related quantities, that is, the linear depolarization ratio  $\delta_p$  (for backward scattering) and the lidar ratio  $S_p$ , show a quite different behaviour. The difference in  $S_p$  is directly evident from  $P_{11}$  (Fig. 5) revealing the reduced backward scattering of the non-spherical particles. Thus, the absolute values of  $S_p$  are significantly higher in case of non-spherical particles. The strong decrease with wavelength is seen in both cases. The linear depolarization ratio  $\delta_p$ , which is related to  $P_{22}/P_{11}$  (right-hand panel in Fig. 5) also shows strong differences: while  $\delta_p = 0$  ( $P_{22}/P_{11} = 1$ ) in case of spheres, spheroids show a significant depolarization between 20.7% and 26.5%. The wavelength dependence is clear between 355 and 1064 nm.

The column labelled ‘ALT’ shows the corresponding values, if the alternative procedure with the wavelength-dependent approach as discussed in the previous section is used. As most of

the values are very close to the reference case, it is evident that the consideration of larger aspect ratios for the large particles only influences the results to a very limited extent.

As already mentioned, the reference case considers particles with  $r < 7.5 \mu\text{m}$  to ensure identical particle ensembles for all wavelengths. However, in view of remote sensing applications, for example, validation activities, larger particles might be relevant, even if their number density is low. For this purpose, we have also performed calculations with extended  $r_{\text{max}}$ . One option is to choose  $r_{\text{max}}$  according to the maximum particle size measured. Weinzierl et al. (2008) demonstrated that in about 70% of the cases the radius of the largest particle measured was between 10 and 20  $\mu\text{m}$ . The radius of particles with number densities of more than  $1 \text{L}^{-1}$  as calculated from the log-normal distributions is  $r_{\text{max}} = 15 \mu\text{m}$ , that is, in the same range. In this paper, we decide to take  $r_{\text{max}} = 10 \mu\text{m}$ : in this case, only for  $\lambda = 355 \text{nm}$  the extension cannot be modelled by the T-matrix method, and the Mie theory must be used for particles  $r > 7.5 \mu\text{m}$ . For the calculation of the ensemble properties we choose the alternative approach as described previously, and the results are shown in column ‘R10’ of Table 4.

It can be seen from ‘R10’ in Table 4 that the extinction coefficient  $\beta_e$  is slightly higher than in the reference case and the Ångström coefficient  $\alpha$  is somewhat lower. This is consistent with the findings known from Mie theory. However, the change of the Ångström coefficient is only marginal. The single scattering albedo is slightly reduced as large particles usually have a smaller  $\omega_0$  than particles with sizes close to the wavelength. The asymmetry parameter  $g$  is higher compared to the reference case because large particles tend to strengthen forward scattering. The lidar ratio  $S_p$  becomes larger, in particular for the short wavelength, when large particles are considered, whereas  $\delta_p$  is only slightly affected. For the sake of completeness it should be mentioned that in case of  $r_{\text{max}} = 15 \mu\text{m}$  the lidar ratio is 46.8 sr at  $\lambda = 532 \text{nm}$ .

Finally, we want to briefly comment on the usefulness of the GOA mentioned at the beginning. For this purpose we have calculated a few selected parameter sets on the basis of the reference case. We applied the code developed by Macke and Mishchenko (1996). As a measure of its potential to extend the size range of our model calculations we use the agreement of the lidar-related parameters with the T-matrix method in the ‘overlap-region’ of  $25 \leq x \leq 135$ . It was found that an extension might be possible for mineral dust particles having large aspect ratios. As a consequence we have considered the ‘true’ shape of these particles (using GOA) instead of replacing them by particles with smaller aspect ratios (‘ALT’ case), but kept  $r_{\text{max}}$  constant. The optical properties do not change significantly: the differences of  $S_p$  are below 0.2 sr, and  $\delta_p$  changes by less than 0.002. If we compare GOA with  $r_{\text{max}} = 15 \mu\text{m}$  with the ‘R10’ case,  $\delta_p$  agrees within 0.005 and the lidar ratio increases between 0.6 and 2.3 sr for  $\lambda = 1064$  and 355 nm, respectively. However, these finding should be considered as preliminary as long as

the potential of GOA has not been thoroughly determined in a quantitative way.

In summary, the main influence of the consideration of large particles concerns the lidar ratio. This is taken into account in Section 5 when we compare model results and measurements.

#### 4.2. Sensitivity studies

In the following, we want to investigate the changes of the optical properties, when the shape, the size distribution or the refractive index is changed. Doing this we can simulate the influence of measurement errors and the influence of the natural variability of particle microphysics. This wide range of sensitivity studies will indicate which optical properties are more or less not influenced by these changes and can be approximated by averages, and which are highly sensitive to changes of certain aerosol properties. They could be candidates for new remote sensing techniques.

*4.2.1. Influence of particle shape.* Let us first discuss the influence of the shape. In this context mainly two questions are in focus. The first concerns the consequences when different particle types are considered: only prolate spheroids as in the reference case, a mixture of prolate and oblate spheroids (50% of each) or only oblate spheroids. As an example of a quite

different particle morphology we also added modelled optical properties of cylinders. This part reflects the uncertainties one normally encounters when no extensive microphysical analysis is available. Furthermore, it is known from several investigations that the shape of mineral particles can be quite variable, whereas only simplified classes of shapes can be modelled here.

The second question is related to the aspect ratio distribution. As already mentioned, in the reference case the distribution measured during SAMUM is used (this issue Kandler et al., 2008). It is interesting to test how optical properties change, if other aspect ratio distributions are assumed. For this purpose the distribution from Dubovik et al. (2006), inverted from measurements of Volten et al. (2001), is applied (see right-hand panel of fig. 13 in their paper). In general the distribution from Dubovik has larger aspect ratios than Kandler's distribution.

Table 5 shows the most important optical properties of particle ensembles consisting of different shapes and aspect ratio distributions. The first column of numbers gives the wavelengths  $\lambda$  followed by the values 'REF' (prolate spheroids only) known from Table 4 as reference. In the 'OP'-column a mixture of prolate and oblate spheroids is used (50% each), whereas in the column labelled 'O' only oblate spheroids are assumed. In the next column ('DUB') the aspect ratio distribution of Dubovik is used for a mixture of prolate and oblate spheroids (again 50%

Table 5. Optical properties for the reference case (REF), for a mixtures of oblate and prolate spheroids (OP), for oblate spheroids (O), for the shape distribution from Dubovik et al. (2006) (DUB) and for prolate cylinders (CYL) for comparison

| Optical property                  | $\lambda$ (nm) | REF    | OP     | O      | DUB    | CYL    |
|-----------------------------------|----------------|--------|--------|--------|--------|--------|
| $\beta_e$<br>( $\text{km}^{-1}$ ) | 355            | 0.1757 | 0.1757 | 0.1757 | 0.1733 | -      |
|                                   | 532            | 0.1742 | 0.1741 | 0.1739 | 0.1709 | 0.1655 |
|                                   | 710            | 0.1720 | 0.1718 | 0.1716 | 0.1691 | -      |
|                                   | 1064           | 0.1696 | 0.1693 | 0.1690 | 0.1675 | -      |
| $\alpha$                          | 355–1064       | 0.032  | 0.034  | 0.035  | 0.031  | -      |
| $\omega_0$                        | 355            | 0.7496 | 0.7487 | 0.7477 | 0.7495 | -      |
|                                   | 532            | 0.8440 | 0.8428 | 0.8417 | 0.8424 | 0.8476 |
|                                   | 710            | 0.9191 | 0.9185 | 0.9178 | 0.9184 | -      |
|                                   | 1064           | 0.9450 | 0.9447 | 0.9444 | 0.9451 | -      |
| $g$                               | 355            | 0.7976 | 0.7924 | 0.7872 | 0.8076 | -      |
|                                   | 532            | 0.7622 | 0.7526 | 0.7430 | 0.7650 | 0.7554 |
|                                   | 710            | 0.7285 | 0.7164 | 0.7043 | 0.7272 | -      |
|                                   | 1064           | 0.7083 | 0.6976 | 0.6869 | 0.7086 | -      |
| $S_p$<br>(sr)                     | 355            | 59.7   | 51.2   | 44.8   | 78.8   | -      |
|                                   | 532            | 42.4   | 34.9   | 29.6   | 50.9   | 20.4   |
|                                   | 710            | 30.8   | 25.4   | 21.5   | 37.0   | -      |
|                                   | 1064           | 28.5   | 23.7   | 20.3   | 34.8   | -      |
| $\delta_p$                        | 355            | 0.2072 | 0.2074 | 0.2076 | 0.2173 | -      |
|                                   | 532            | 0.2348 | 0.2447 | 0.2517 | 0.2383 | 0.2047 |
|                                   | 710            | 0.2432 | 0.2538 | 0.2613 | 0.2438 | -      |
|                                   | 1064           | 0.2650 | 0.2633 | 0.2620 | 0.2586 | -      |

Table 6. Assignment of aspect ratios to  $l/d$  of cylinders

| $l/d$          | 1.0 | 1.4      | 1.8      | 2.2      | 2.6           |
|----------------|-----|----------|----------|----------|---------------|
| $\varepsilon'$ | 1.2 | 1.4, 1.6 | 1.8, 2.0 | 2.2, 2.4 | 2.6, 2.8, 3.0 |

each). Finally, the results for an ensemble of prolate cylinders derived from the measured aspect ratio distribution (see Table 1) are given, however, only for  $\lambda = 532$  nm.

For all cases the same size distribution and the same refractive index are assumed. With respect to the aspect ratio distribution, cylinders are described by their diameter  $d$  and length  $l$ . The aspect ratio is interpreted as  $l/d$  (as shown in Table 6). To save computer time, we have reduced the numbers of 10 aspect ratio classes (used for the spheroids) to 5  $l/d$ -classes of cylinders.

With respect to the extinction coefficient  $\beta_e$  the difference between oblate and prolate spheroids increases with wavelength and is about 0.4% at 1064 nm. As a consequence the Ångström parameter is  $\alpha = 0.035$  for oblate spheroids, while it is  $\alpha = 0.032$  in the reference case; this difference is very small. Small differences are also found for  $\omega_0$ . The relative sensitivity of the asymmetry parameter  $g$  is in the range of 2% with the largest effect at long wavelengths. In summary, the effect of prolate and oblate spheroids on these quantities is similar to the effect we find when we compare the reference case with spherical particles.

When the aspect ratio distribution of Dubovik et al. (2006) is applied, the extinction is about 1.4% lower than in the reference case. This effect is due to the extinction of particles smaller than the wavelength. The extinction of these particles decreases with increasing asphericity (Zakharova and Mishchenko, 2000). At most wavelengths  $\omega_0$  and  $g$  are comparable to the ones found in the previous cases.

In case of cylinders  $\omega_0$  and  $g$  again are in the same range as in the previous cases, only the extinction coefficient  $\beta_e$  is lower by 5% when compared to the spheroid cases.

Again, the lidar-related quantities show a much stronger sensitivity to particle shape. If we compare the reference case to oblate spheroids,  $S_p$  differs between 15 sr ( $\lambda = 355$  nm) and approximately 8 sr ( $\lambda = 1064$  nm), which is not negligible. When the aspect ratio distribution from Dubovik is applied  $S_p$  gets significantly higher compared to the reference case, particularly at short wavelengths where the difference can be as high as 19 sr. In case of cylinders, the lidar ratio is significantly lower (20.4 sr) which is quite close to the case of spherical particles (21.3 sr). One possible reason, that cylinders are relative effective backscatters, is the 90° angle between the ground plate and the sides. The linear depolarization ratio  $\delta_p$  varies typically by 0.01 when the different spheroid cases are considered, but is significantly lower ( $\delta_p = 0.205$ ) in case of cylinders.

Finally, we estimate the range of uncertainty due to the unknown shape of the particles. This is done for  $\lambda = 532$  nm by considering the variability shown in Table 5. As a result, we find for the single scattering albedo  $\omega_0 = 0.844 \pm 0.003$ , the asymmetry parameter  $g = 0.762 \pm 0.012$ , and the Ångström coefficient  $\alpha = 0.032 \pm 0.003$ . The single scattering albedo increases with wavelength, whereas the asymmetry parameter decreases with wavelength. The range of the lidar ratio is  $S_p = 42$  sr  $\pm 10$  sr, the mean linear depolarization ratio  $\delta_p = 0.235 \pm 0.012$  without consideration of cylinders. The lidar ratio decreases with wavelength, whereas  $\delta_p$  increases with  $\lambda$ . It is obvious that the variability of the lidar-related parameters is much more pronounced than the variability of the quantities that are integrated over the scattering angle ( $\omega_0, g, \alpha$ ).

**4.2.2. Influence of particle size distribution.** The influence of the particle size is investigated by using size distributions measured at different days and different flight levels by the in situ instruments onboard of the Falcon. This approach is preferred to a purely theoretical estimate of the variability. The results are shown in Table 7. The different columns refer to different assumption on the particle shape. Column ‘S’ assumes spheres for comparison, ‘P’ assumes only prolate spheroids as it is the case in the reference case and the column (‘OP’) assumes a mixture of 50% oblate and 50% prolate spheroids. Note, that only optical properties for  $\lambda = 532$  nm are given here. The shape distribution and the refractive index are the same as for the reference case.

As the size distributions are given in absolute numbers, the extinction coefficients from different meteorological conditions are hard to compare—they reflect the varying aerosol load rather than changes in optical properties. For this purpose, the Ångström coefficient is the better indicator of the variability of the optical properties. As a consequence, only this number—calculated for the spectral range from 355 to 1064 nm—is considered here. The Ångström coefficient  $\alpha$  is close to zero in all cases indicating that large particles are dominating the radiative impact. It is obvious that the variations of  $\alpha$  due to different size distributions—though small—are larger than the differences caused by the particle shape. The variability of the single scattering albedo  $\omega_0$  lies in the range of 0.81–0.85 at  $\lambda = 532$  nm. Again, the size-induced changes are larger than the variability due to different shape assumptions, whereas the variation of  $g$  due to changes in size or shape are of similar magnitude. The spherical versus non-spherical differences are small in all cases for  $\alpha$ ,  $\omega_0$  and  $g$ . The range of variation of the lidar ratio can be as large as 16 sr when the different measured size distributions are considered. For  $\delta_p$  the variation is in the range of 0.03. For both lidar-related quantities the changes due to size or shape are comparable and significant.

**4.2.3. Influence of refractive index.** The influence of the refractive index on the optical properties is investigated separately for changes of the real and the imaginary parts in relation to the

Table 7. Optical properties ( $\lambda = 532$  nm and  $\alpha$  from 355 to 1064 nm) assuming particles to be spheres (S), prolate spheroids (P) or oblate and prolate spheroids in equal shares (OP). ‘Pm’ is for a different refractive index  $m$  (for details see text). Different size distributions are indicated by the ID of the flight level (e.g. L2) and the date of the measurements. The altitude of the flight levels and the effective radii of the distributions are given in parenthesis

|                          | Level                   | S      | P      | OP     | Pm     |
|--------------------------|-------------------------|--------|--------|--------|--------|
| $\alpha$                 | 19.5. L2 (4.85 km)      | -0.011 | -0.012 | -0.010 | -0.012 |
|                          | 19.5. L3 (3.25 km)      | 0.083  | 0.087  | 0.088  | 0.086  |
|                          | 22.5. L4 (3.19 km)      | 0.059  | 0.057  | 0.058  | 0.058  |
|                          | 28.5. L12 (2.19 km)     | -0.007 | -0.008 | -0.006 | -0.007 |
|                          | 3.6. L6 (3.82 km)       | 0.092  | 0.085  | 0.087  | 0.088  |
|                          | 3.6. L7 (2.49 km)       | 0.022  | 0.021  | 0.023  | 0.023  |
|                          | 3.6. L8 (2.36 km)       | -0.018 | -0.019 | -0.017 | -0.018 |
|                          | 4.6. L4 (2.90 km)       | -0.048 | -0.048 | -0.046 | -0.047 |
|                          | 19.5. L2 (2.45 $\mu$ m) | 0.8394 | 0.8392 | 0.8381 | 0.8415 |
|                          | 19.5. L3 (2.32 $\mu$ m) | 0.8522 | 0.8515 | 0.8503 | 0.8498 |
| 22.5. L4 (2.86 $\mu$ m)  | 0.8162                  | 0.8151 | 0.8137 | 0.8137 |        |
| 28.5. L12 (2.05 $\mu$ m) | 0.8517                  | 0.8516 | 0.8506 | 0.9094 |        |
| 3.6. L6 (1.16 $\mu$ m)   | 0.8929                  | 0.8931 | 0.8926 | 0.9313 |        |
| 3.6. L7 (2.43 $\mu$ m)   | 0.8331                  | 0.8324 | 0.8312 | 0.9156 |        |
| 3.6. L8 (2.65 $\mu$ m)   | 0.8236                  | 0.8230 | 0.8217 | 0.9064 |        |
| 4.6. L4 (2.29 $\mu$ m)   | 0.8434                  | 0.8434 | 0.8424 | 0.9217 |        |
| $\omega_0$               | 19.5. L2                | 0.7679 | 0.7649 | 0.7548 | 0.7641 |
|                          | 19.5. L3                | 0.7596 | 0.7585 | 0.7495 | 0.7589 |
|                          | 22.5. L4                | 0.7795 | 0.7766 | 0.7677 | 0.7768 |
|                          | 28.5. L12               | 0.7604 | 0.7574 | 0.7466 | 0.7389 |
|                          | 3.6. L6                 | 0.7250 | 0.7220 | 0.7112 | 0.7103 |
|                          | 3.6. L7                 | 0.7715 | 0.7680 | 0.7577 | 0.7402 |
|                          | 3.6. L8                 | 0.7802 | 0.7764 | 0.7659 | 0.7479 |
|                          | 4.6. L4                 | 0.7670 | 0.7634 | 0.7524 | 0.7372 |
|                          | 19.5. L2                | 17.8   | 41.2   | 33.6   | 40.8   |
|                          | 19.5. L3                | 20.1   | 43.6   | 36.2   | 43.8   |
| 22.5. L4                 | 22.2                    | 49.0   | 40.9   | 49.1   |        |
| 28.5. L12                | 17.0                    | 38.9   | 31.3   | 31.4   |        |
| 3.6. L6                  | 14.3                    | 33.4   | 26.7   | 29.2   |        |
| 3.6. L7                  | 19.3                    | 43.5   | 35.4   | 30.8   |        |
| 3.6. L8                  | 19.7                    | 44.1   | 35.8   | 31.2   |        |
| 4.6. L4                  | 16.8                    | 39.2   | 31.6   | 29.2   |        |
| $S_p$<br>(sr)            | 19.5. L2                | 0      | 0.2400 | 0.2490 | 0.2397 |
|                          | 19.5. L3                | 0      | 0.2288 | 0.2397 | 0.2285 |
|                          | 22.5. L4                | 0      | 0.2170 | 0.2357 | 0.2165 |
|                          | 28.5. L12               | 0      | 0.2426 | 0.2518 | 0.2410 |
|                          | 3.6. L6                 | 0      | 0.2455 | 0.2462 | 0.2502 |
|                          | 3.6. L7                 | 0      | 0.2304 | 0.2463 | 0.2228 |
|                          | 3.6. L8                 | 0      | 0.2334 | 0.2504 | 0.2239 |
|                          | 4.6. L4                 | 0      | 0.2462 | 0.2551 | 0.2398 |

values of 19 May,  $m = 1.56 + 0.0043 i$ . Again, only  $\lambda = 532$  nm is considered.

The real part of modes 2–4 (see Table 3) is changed to 1.52 and 1.60, that is, a deviation from the measured one of  $\pm 0.04$  is

Table 8. Optical properties ( $\lambda = 532$  nm) for different refractive indices, assuming spheres (S) and prolate spheroids (P)

|                                   | Refr. index      | S      | P      |
|-----------------------------------|------------------|--------|--------|
| $\beta_e$<br>( $\text{km}^{-1}$ ) | REF case         | 0.1739 | 0.1742 |
|                                   | 1.52 + 0.0043 i  | 0.1741 | 0.1744 |
|                                   | 1.60 + 0.0043 i  | 0.1736 | 0.1740 |
|                                   | 1.56 + 0.00215 i | 0.1739 | 0.1743 |
|                                   | 1.56 + 0.0086 i  | 0.1738 | 0.1741 |
| $\omega_0$                        | REF case         | 0.8444 | 0.8440 |
|                                   | 1.52 + 0.0043 i  | 0.8451 | 0.8456 |
|                                   | 1.60 + 0.0043 i  | 0.8438 | 0.8424 |
|                                   | 1.56 + 0.00215 i | 0.9059 | 0.9040 |
|                                   | 1.56 + 0.0086 i  | 0.7684 | 0.7710 |
| $g$                               | REF case         | 0.7642 | 0.7622 |
|                                   | 1.52 + 0.0043 i  | 0.7732 | 0.7721 |
|                                   | 1.60 + 0.0043 i  | 0.7558 | 0.7529 |
|                                   | 1.56 + 0.00215 i | 0.7486 | 0.7404 |
|                                   | 1.56 + 0.0086 i  | 0.7849 | 0.7879 |
| $S_p$<br>(sr)                     | REF case         | 18.9   | 42.4   |
|                                   | 1.52 + 0.0043 i  | 26.8   | 48.8   |
|                                   | 1.60 + 0.0043 i  | 12.6   | 37.2   |
|                                   | 1.56 + 0.00215 i | 14.7   | 32.2   |
|                                   | 1.56 + 0.0086 i  | 26.9   | 60.7   |
| $\delta_p$                        | REF case         | 0      | 0.2348 |
|                                   | 1.52 + 0.0043 i  | 0      | 0.2604 |
|                                   | 1.60 + 0.0043 i  | 0      | 0.2109 |
|                                   | 1.56 + 0.00215 i | 0      | 0.2247 |
|                                   | 1.56 + 0.0086 i  | 0      | 0.2383 |

investigated. This deviation is comparable to the natural variability found by Dubovik et al. (2002). The imaginary part remained unchanged at  $m_i = 0.0043$ . When we change the imaginary part to half and twice of this value, the real part of the refractive index is held constant. In all cases shown here the refractive index of mode 1 (the non-absorbing fraction) is not modified.

The results for the different refractive indices are shown in Table 8, ‘S’ is for spherical particles, ‘P’ for prolate spheroids. It indicates that the extinction is almost independent of  $m$ .  $\omega_0$  strongly depends on the imaginary part of  $m$ . The differences of  $\omega_0$  between the spheres and prolate spheroids are comparably small. The asymmetry parameter  $g$  changes with  $m_r$  and  $m_i$  with variations up to 0.02. The lidar ratio  $S_p$  shows significant dependence on both the real and the imaginary parts of the refractive index. For non-spherical particles it strongly increases with  $m_i$  and decreases with  $m_r$ .  $\delta_p$  always lays in the range of 0.21–0.26, showing especially a clear and significant dependence on  $m_r$ .

4.2.4. Day-to-day variability. In the previous paragraphs, we have discussed the changes of the optical properties when one microphysical parameter has been varied and all other parameters have been held constant. As a full characterization of shape,

size and refractive index is not available for all occasions—and will never be under normal experimental conditions—we have estimated the natural day-to-day variability by simulations shown in the rightmost column ‘Pm’ of Table 7. Here—more realistically—we take into account the actually measured size distributions and refractive indices for the indicated times and levels; only the shape distribution is held constant according to Table 1. For 19 and 22 May the aerosol is characterized by a large imaginary part of the refractive index, whereas in June  $m_i$  is small compared to the reference case. Here, the lidar ratio is significantly lower. This is consistent with the results shown in Table 8.

It certainly is risky to postulate averaged values to be climatological means for Saharan dust as the number of days is very limited and the representativeness of the days is unknown. So we rather give the variation ranges. If we consider the 5 d (19, 22, 28 May and 3, 4 June) we get Ångström coefficients  $\alpha$  in the range between  $-0.05$  and  $0.1$ . For the single scattering albedo we find  $0.81 \leq \omega_0 \leq 0.94$ , for the asymmetry parameter  $0.71 \leq g \leq 0.78$ , for the lidar ratio  $29 \leq S_p \leq 50$  sr and  $0.215 \leq \delta_p \leq 0.25$  for the depolarization ratio. These values are for  $\lambda = 532$  nm and for particles not larger than  $r = 7.5$   $\mu\text{m}$ .

## 5. Comparison with measurements

We have calculated optical properties of an aerosol ensemble that has been characterized by in situ measurements of 19 May 2006, around noon in the vicinity of Ouarzazate. Based on these data it is possible to compare the results of our numerical simulations with corresponding measurements. In this context we only briefly discuss the Ångström coefficient  $\alpha$ , but mainly concentrate on the lidar-related variables  $S_p$  and  $\delta_p$ .

It was already mentioned that particles larger than  $r = 7.5$   $\mu\text{m}$  are not considered in the reference case and the subsequent sensitivity studies, since the applicability of the T-matrix method is limited to particles up to this radius at the shortest wavelength (355 nm). However, when we focus on  $\lambda = 532$  nm, we can extend the range of particle radius to  $r_{\text{max}} = 10$   $\mu\text{m}$  as these particles might influence remote sensing techniques, for example, the lidar measurements. Including large particles we find for  $\lambda = 532$  nm that the single scattering albedo is  $\omega_0 = 0.83$ , the asymmetry parameter  $g = 0.77$  and the Ångström coefficient  $\alpha = 0.027$  (see ‘R10’ in Table 4). The spectral behaviour in general does not change compared to the reference case. The lidar ratio  $S_p$  is somewhat larger when larger particles are considered ( $S_p = 45$  sr compared to 42 sr), whereas the depolarization ( $\delta_p = 0.233$ ) is almost unchanged.

Both measurements and simulations of the Ångström coefficient show values close to zero indicating the presence of large particles. Detailed comparisons with lidar measurements and sun photometer retrievals must, however, be aware of differences in the spectral range, temporal and spatial resolution (sun photometers provide columnar values). For the different days,

considered in our simulations, we found Ångström coefficients in the interval  $-0.05 \leq \alpha \leq 0.1$  (355–1064 nm). The values are slightly different ( $-0.05 \leq \alpha \leq 0.16$ ), if we limit the spectral range to the range where lidar derived extinction coefficients are available (355–532 nm). For the 355–532 nm range, Tesche et al. (2008) found an average over several days of  $\alpha \approx 0.06$  from lidar measurements with variations with height between 0 and 0.1. Toledano et al. (2008) found from sun photometer measurements for the dust cases a vertically averaged  $\alpha$  in the order of 0.15–0.32 (spectral range 440–870 nm).

A recent overview by Müller et al. (2007) report lidar ratios of  $55 \pm 6$  sr at  $\lambda = 355$  nm, and similar values for 532 nm based on preliminary results from Raman lidar data during SAMUM. Measurements in the framework of EARLINET show slightly larger lidar ratios ( $59 \pm 11$  sr) at 532 nm for Saharan dust layer aerosols over Europe (Ansmann et al., 2003), that is, aerosols that are not close to their source regions as during SAMUM. For desert dust, measured during INDOEX over Saudi Arabia, lidar ratios are significantly lower ( $38 \pm 5$  sr), but also wavelength independent.

A comparison of the lidar ratio for 19 May is shown in Fig. 6. For this day, in situ measurements at two levels are available (4.85 km around 11:30 UT and 3.25 km around 11:55 UT, confer Table 7) and lidar measurements at 11:08 UT, averaged over 5 min (corresponding to approximately 60 km of flight track). According to the fact that both in situ measurements are quite similar and the time difference is less than 1 h, the conditions for an intercomparison are very promising. The full line shows the

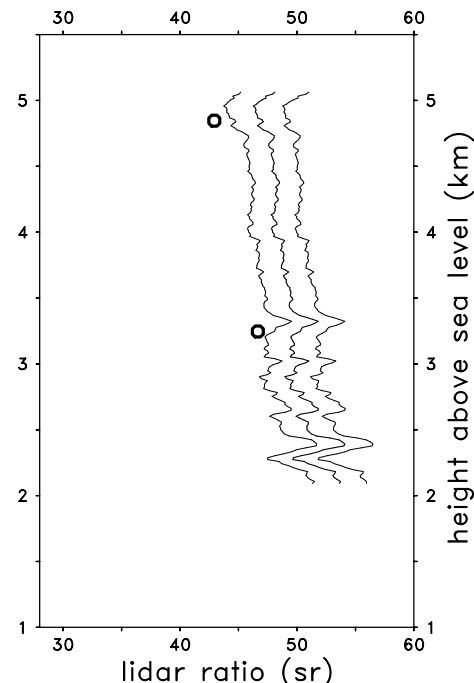


Fig. 6. HSRL measurement of the lidar ratio at  $\lambda = 532$   $\mu\text{m}$  on 19 May 2006 compared to modelled lidar ratio.

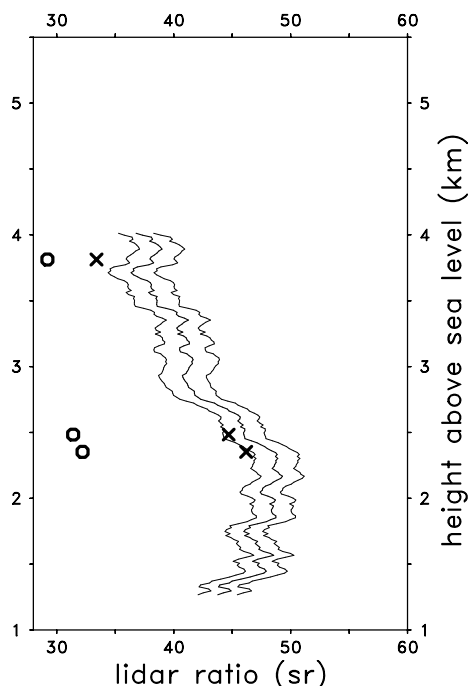


Fig. 7. HSRL measurement of the lidar ratio at  $\lambda = 532$  nm on 3 June 2006 compared to modelled lidar ratio: refractive index from the in situ measurements (circles) and from the reference case (crosses).

vertical profile of  $S_p$  for 532 nm as derived from the high spectral resolution lidar when the Falcon crossed Ouarzazate in 9.4 km height. The left and right lines indicate the error range of the retrieval. The circles mark the calculated lidar ratios when the size distributions and the refractive indices as measured at the corresponding levels are used as input. For 3.25 km height the agreement is good: 46.7 sr from the simulations versus  $50.3 \pm 2.2$  sr from the HSRL. For 4.85 km the agreement is only slightly worse when we compare the modelled value (42.9 sr) with the measured value ( $47.0 \pm 2.4$  sr).

A similar comparison is performed for 3 June (Fig. 7). Here, in situ measurements between 08:57 and 09:04 UT at three levels (3.82, 2.49 and 2.36 km, respectively) over Ouarzazate are available. It is noteworthy that the imaginary part of the refractive indices are much lower than on 19 May, namely between 0.0025 and 0.0017. The lidar measurements have been performed at 07:41 UT over Tinfou. As a consequence, the temporal difference is more than 1 h and the spatial difference more than 100 km. Furthermore, the aerosol layer is not as homogeneous as on 19 May; in particular a two layer structure with a internal boundary at about 2.75 km is obvious. For these reasons the conditions for an intercomparison are less favourable. The HSRL shows  $S_p$  between 44 and 48 sr in the lower part of the layer and lidar ratios in the order of 38 sr in the upper part. The simulations, based on the size distributions and refractive indices measured approximately 1 h later, show significantly lower lidar ratios: they are between 29 and 32 sr.

Table 9. Depolarization ratio as available from lidar measurements; 19 May in 3.25 km height

| $\lambda$ (nm) | $\delta_p$      | Instrument |
|----------------|-----------------|------------|
| 355            | $0.25 \pm 0.08$ | POLIS      |
| 532            | $0.30 \pm 0.03$ | HSRL       |
| 532            | $0.31 \pm 0.02$ | MULIS      |
| 1064           | $0.27 \pm 0.04$ | HSRL       |

These discrepancies are drastically reduced if we apply different refractive indices. If we assume a higher imaginary part of, for example, 0.0043 as it is the case in the reference case, the agreement is much better: it almost perfectly fits to the lidar retrieval in the lower part (46.2 and 44.6 sr as shown by the crosses in Fig. 7), and is only slightly smaller at 3.8 km height (33.4 vs. 38 sr of the measurements). So, if we accept that the refractive index can change in this range during 80 min, the discrepancy between measurements and simulations disappears. However, this statement is one explanation out of several. It could also be possible that the particle shapes are somewhat different.

Measurements of the depolarization ratio of mineral dust have been very rare before SAMUM and exhibits large uncertainties and/or a large variability. For 532 and 710 nm they are found to be in the range of 0.1 and 0.25 for long-range transported dust (Müller et al., 2007). The measured  $\delta_p$  for 19 May are summarized in Table 9, they included data for  $\lambda = 355$  nm (POLIS),  $\lambda = 532$  nm (MULIS and HSRL) and  $\lambda = 1064$  nm (HSRL); data for  $\lambda = 710$  nm are not available for that day.

The measured  $\delta_p$  is in the range between 0.25 and 0.31. For the 355 nm wavelength, the uncertainty is quite large, mainly because of the dominant contribution of molecular backscattering compared to the aerosol backscattering. The agreement of both lidars at  $\lambda = 532$  nm is very good. At  $\lambda = 1064$  nm,  $\delta_p$  is between the values of the other wavelengths. So, a monotonic change of  $\delta_p$  is not observed.

Comparisons with the modelled  $\delta_p$  show that all depolarization ratios are in the same range, but the measured  $\delta_p$  are larger than the simulated values: at 355 nm the simulations are lower by 0.05, at 532 nm by 0.07. At 1064 nm, the agreement is good. The increase of the depolarization ratio with wavelength as found from the simulations cannot be resolved by the measurements.

In summary, if we compare  $\delta_p$  and  $S_p$ , the agreement in some cases is very good (lidar ratio at 532 nm for 19 May, and depolarization ratio at 1064 nm), in other cases the agreement is relatively poor, for example, for the depolarization ratio at 532 nm on 19 May, or the lidar ratio on 3 June.

The reasons of these discrepancies become obvious if we consider Fig. 8. Here, the lidar ratio and linear depolarization ratio at 532 nm for different refractive indices—real part between 1.48 and 1.60 and imaginary part between 0 and 0.0086—is shown. The non-absorbing case,  $m_i = 0$ , certainly is unrealistic

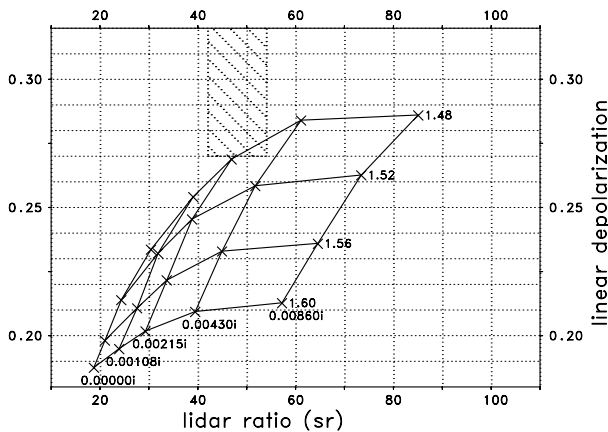


Fig. 8. Lidar ratio and linear depolarization ratio for different refractive indices (real and imaginary parts); shape distribution by Kandler, prolate spheroids;  $\lambda = 532$  nm.

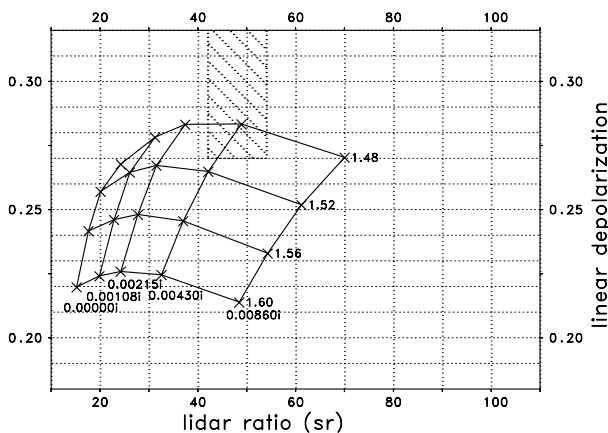


Fig. 9. Same as Fig. 8, but mixture of prolate and oblate spheroids (50 each).

and is only added to illustrate the theoretically lowest values. The simulations are based on the R10 case, that is,  $r_{\max} = 10 \mu\text{m}$  is selected, the aspect ratio distribution of Table 1 is taken and it is assumed that all particles are prolate spheroids. It can be seen that the hatched area that visualizes the most likely range of measurements of May 19., only marginally overlap with the modelled  $(S_p, \delta_p)$ -pairs. Only if we assume quite low real part of the refractive index, an agreement could be possible.

If the assumption of an aerosol ensemble consisting of prolate spheroids only is dropped and we model a mixture of prolate and oblate spheroids, the agreement between measurements and simulations becomes somewhat better (see Fig. 9). Again, the simulations suggest that the real part of the refractive index must be lower than derived from the in situ measurements, but the overlap of the range of measurements (hatched area) and the simulations is much larger.

If we assume as before that the particle ensemble can be approximated by prolate and oblate spheroids in equal parts, but that the aspect ratio distribution is different, the simulations show

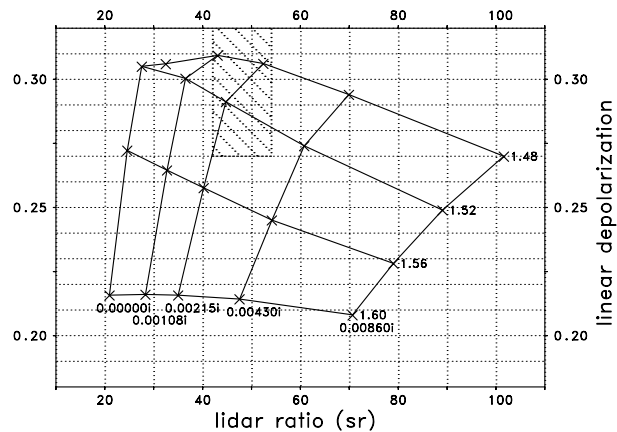


Fig. 10. Same as Fig. 9, but shape distribution by Dubovik.

a very good agreement with the measurements. This is shown in Fig. 10. Here, we again use the aspect ratio distribution of Dubovik et al. (2006) with a larger frequency of particles with large  $\varepsilon'$ . Under these conditions the measurements suggest a refractive index that is very close to the in situ measurements and the agreement is perfect if the real and the imaginary parts of  $m$  are slightly lower.

It is known that the determination of the shape of the particles is difficult, in particular, as only two-dimensional images are available. It is also known that their approximation by idealized types such as spheroids must be critical because an unknown number of particles might significantly deviate from a 'smooth' morphology. Finally, and as a conclusion of the former, it is obvious that the description of the particle ensemble by a realistic  $\varepsilon'$ -distribution must be difficult. As it is shown in Figs. 8–10, these uncertainties have significant consequences on the  $(S_p, \delta_p)$ -pairs for given refractive indices. Note, that these figures do not account for variations of the size distribution.

It is expected that calculations with modified size distributions—motivated by possible measurement errors or the natural variability—will alter the above distribution of  $\delta_p$  and  $S_p$ . By modifications of either one of the modal radii of the log-normal distribution, their width or their relative contribution to the total number density, an even better agreement might be found. Due to the large number of degrees of freedom this investigation is postponed to a later stage.

As a consequence, a strict validation can only be achieved if the size and the shape distribution of the particles is characterized precisely. It is obvious that this cannot be performed in all cases; the only solution might be to increase the number of measurements to establish a reliable climatology, which is of course a very costly effort.

## 6. Summary and conclusions

Saharan Mineral Dust Experiment has offered for the first time the chance to investigate the wavelength dependence of the

linear depolarization ratio (see companion paper by Freudenthaler et al., 2008, this issue). It was the goal of this paper to perform the corresponding numerical experiments. Special emphasis was put on the linear depolarization ratio  $\delta_p$  and the lidar ratio  $S_p$ , but, optical properties relevant for radiative transport modelling, for example, the single scattering albedo or the Ångström coefficient, were provided as well. The numerical simulations applied the T-Matrix approach for spheroids.

Size distributions, refractive indices and information on the shape of the particles are provided by in situ measurements. The first critical issue in this context is that the determination of the refractive index implicitly is based on an inversion of measurements of the absorption at three wavelengths (using Mie theory) and the assumption that the particles consist of a mixture of quartz, kaolinite and haematite Petzold et al., (2008, this issue). As the refractive index of these components is quite different, in particular the imaginary part, even small changes in the composition change the mean refractive index of the particles that is used for our calculations. For example, a larger amount of kaolinite at the expense of haematite would drastically reduce the imaginary part at  $\lambda = 355$  nm. If we assume 0.2% instead of 0.44% of haematite (32.2% instead of 32.0% of kaolinite),  $m_i$  will be 0.0052 at  $\lambda=355$  nm instead of 0.0078. At  $\lambda = 532$  nm the reduction would also be significant (0.0031 vs. 0.0043). The situation is even more complicated as the dust aerosol can be a mixture of more than three components (Kandler et al., 2008) and the natural variability of the particle composition is expected to be large. The second crucial point is the approximation of the particles' morphology by simplified shapes. The common approach is to assume rotationally invariant particles that are described by the aspect ratio. Some particles might, however, exhibit very specific features and cannot be treated by such idealized types. Based on this problem, the estimation of the relative frequency of specific aspect ratios—required for the numerical simulations—is even more difficult. Needless to mention that a comprehensive analysis of all particles at any time is unrealistic.

As a consequence, the characterization of the mineral dust in the framework of SAMUM was certainly the best possible way, but a range of uncertainty of the microphysical properties should be kept in mind. For example, the imaginary part of the refractive index varied between 0.0016 and 0.0048 for  $\lambda = 532$  nm during the four weeks of observation. It is doubtful whether a significant improvement can be achieved in future as it is unrealistic to determine these parameters on a routine basis.

Under these conditions the agreement between simulations and measurements is good: the lidar ratio of mineral dust was found to be most likely in the range of 40–60 sr for  $\lambda = 532$  nm, if we restrict to  $m_i$  near 0.0043, and the depolarization ratio  $\delta_p$  between 0.2 and 0.31. The later range is in good agreement with the observed range within SAMUM (Freudenthaler et al., 2008). From our calculations we expect that  $\delta_p$  slightly increases with wavelength. At the present state this could not be confirmed by measurements as they do not retrieve  $\delta_p$  with the required accu-

racy in the order of  $\pm 0.01$ . On the other hand, the measurements do not disprove the simulations. As a rule of thumb we found that  $\delta_p$  does not depend significantly on  $m_i$ , increases with decreasing real part  $m_r$  and the lidar ratio increases with increasing  $m_i$  and decreasing  $m_r$ . These findings could not be validated in the frame of SAMUM but can give hints for subsequent closure experiments.

As next steps it is planned to further characterize the microphysical properties of mineral dust aerosols. If more particles will be analysed, 'typical' properties and the range of their variations can be assessed more reliably. In parallel, we will continue to numerically investigate the influence of different particle shapes and size distributions on the optical properties. In this context we will also consider the GOA and recent developments of the T-matrix method that allows to model particles with complex shapes including 'mildly' concave morphologies (see e.g. Doicu et al., 2006).

## 7. Acknowledgments

The authors are grateful to Oleg Dubovik for useful comments and to Michael Mishchenko for the provision of his T-Matrix code.

The present study was supported by the German Research Foundation within the Research Group SAMUM.

## References

- Ansmann, A., Bösenberg, J., Chaikovsky, A., Comerón, A., Eckhardt, S. and co-authors. 2003. Long-range transport of Saharan dust to northern Europe: the 11–16 October 2001 outbreak observed with EARLINET. *J. Geophys. Res. (Atmos.)* **108**. doi:10.1029/2003JD003757.
- Arakawa, E. T., Tuminello, P. S., Khara, B. N., Millham, M. E., Authier, S. and co-authors. 1997. Measurement of optical properties of small particles. *NASA Ames Research Center, Report No.: CONF-9706222, DE98-001913, ORNL CP-95872*.
- Doicu, A., Wriedt, T. and Eremin, Y. A. 2006. *Light Scattering by Systems of Particles, Null-Field Method with Discrete Sources—Theory and Programs*. Springer Verlag, Berlin, Heidelberg, New York.
- Dubovik, O., Holben, B., Eck, T. F., Smirnov, A., Kaufman, Y. J. and co-authors. 2002. Variability of absorption and optical properties of key aerosol types observed in worldwide locations. *J. Atmos. Sci.* **59**, 590–608.
- Dubovik, O., Sinyuk, A., Lapyonok, T., Holben, B. N., Mishchenko, M. and co-authors. 2006. Application of spheroid models to account for aerosol particle nonsphericity in remote sensing of desert dust. *J. Geophys. Res. (Atmos.)*, **111**, doi:10.1029/2005JD006619.
- Fiebig, M. 2001. *The tropospheric aerosol in mid-latitudes - microphysics, optics and climate forcing using the example of the field study LACE 98. (Das troposphärische Aerosol in mittleren Breiten - Mikrophysik, Optik und Klimaantrieb am Beispiel der Feldstudie LACE 98)*. PhD thesis. Faculty for physics, LMU Munich (Dissertation der Fakultät für Physik der Ludwig-Maximilians-Universität München).

- Freudenthaler, V., Esselborn, M., Wiegner, M., Heese, B., Tesche, M. and co-authors. 2008. Depolarization-ratio profiling at several wavelengths in pure Saharan dust during SAMUM. *Tellus* **61B**, doi: 10.1111/j.1600-0889.2008.00396.x.
- Kandler, K., Deutscher, C., Ebert, M., Hofmann, H., Jäckel, S. and co-authors. 2008. Size distributions, mass concentrations, chemical and mineralogical composition, and derived optical parameters of the boundary layer aerosol at Tinfou, Morocco, during SAMUM 2006. *Tellus* **61B**, doi: 10.1111/j.1600-0889.2008.00385.x.
- Macke, A. and Mishchenko, M. I. 1996. Applicability of regular particle shapes in light scattering calculations for atmospheric ice particles. *Appl. Opt.* **35**, 4291–4296.
- Mishchenko, M. I. and Travis, L. D. 1998. Capabilities and limitations of a current Fortran implementation of the T-Matrix method for randomly oriented, rotationally symmetric scatterers. *J. Quant. Spectrosc. Radiat. Transfer* **60**, 309–324.
- Mishchenko, M. I., Travis, L. D., Kahn, R. A. and West, R. A. 1997. Modeling phase functions for dust-like tropospheric aerosols using a shape mixture of randomly oriented polydisperse spheroids. *J. Geophys. Res.* **102**, 13 543–13 553.
- Müller, D., Ansmann, A., Mattis, I., Tesche, M., Wandinger, U. and co-authors. 2007. Aerosol-type-dependent lidar ratios observed with Raman lidar. *J. Geophys. Res. (Atmos.)* **112**, doi:10.1029/2006JD008292.
- Nicolae, D. N., Talianu, C., Ciobanu, M., Babin, V. and Radu, C. 2004. Effects of nonsphericity on depolarization LIDAR data analysis. In: *22nd International Laser Radar Conference (ILRC 2004)*, (eds. G. Pappalardo and A. Amodeo). Vol. 561, ESA Special Publication, 515 pp.
- Nousiainen, T. and Vermeulen, K. 2003. Comparison of measured single-scattering matrix of feldspar with T-matrix simulations using spheroids. *J. Quant. Spectrosc. Radiat. Transfer* **79**, 1031–1042.
- Petzold, A., Rasp, K., Weinzierl, B., Esselborn, M., Hamburger, T. and co-authors. 2008. Saharan dust absorption and refractive index from aircraft-based observations during SAMUM 2006. *Tellus* **61B**, doi: 10.1111/j.1600-0889.2008.00383.x.
- Purcell, E. M. and Pennypacker, C. R. 1973. Scattering and absorption of light by nonspherical dielectric grains. *Astrophys. J.* **186**, 705–714.
- Sokolik, I. N. and Toon, O. B. 1999. Incorporation of mineralogical composition into models of the radiative properties of mineral aerosol from UV to IR wavelengths. *J. Geophys. Res.* **104**, 9423–9444, doi:10.1029/1998JD200048.
- Solomon, S., Qin, D., Manning, M., Chen, Z., Marquis, M. and co-editors. 2007. *The Physical Science Basis. Contribution of Working Group I to the Fourth Assessment Report of the Intergovernmental Panel on Climate Change*. Cambridge University Press, Cambridge, United Kingdom and New York, 996 pp.
- Tesche, M., Ansmann, A., Müller, D., Althausen, D., Mattis, I. and co-authors. 2008. Vertical profiling of Saharan dust with Raman lidars and airborne HSRL in southern Morocco during SAMUM. *Tellus* **61B**, doi: 10.1111/j.1600-0889.2008.00390.x.
- Toledano, C., Wiegner, M., Garhammer, M., Seefeldner, M., Gasteiger, J. and co-authors. 2008. Spectral aerosol optical depth characterization of desert dust during SAMUM 2006. *Tellus* **61B**, doi: 10.1111/j.1600-0889.2008.00382.x.
- Veihelmann, B., Volten, H. and van der Zande, W. J. 2004. Light reflected by an atmosphere containing irregular mineral dust aerosol. *Geophys. Res. Lett.* **31**L04113, doi:10.1029/2003GL018229.
- Virkkula, A., Ahlquist, N. C., Covert, D. S., Arnott, W. P., Sheridan, P. J. and co-authors. 2005. Modification, calibration and a field test of an instrument for measuring light absorption by particles. *Aerosol Sci. Technol.* **39**, 68–83, doi:10.1080/027868290901963.
- Volten, H., Munoz, O., Rol, E., de Haau, J. F., Vassen, W. and co-authors. 2001. Scattering matrices of mineral aerosol particles at 441.6 nm and 632.8 nm. *J. Geophys. Res.* **106**, 17 375–17 401.
- Waterman, P. C. 1971. Symmetry, unity, and geometry in electromagnetic scattering. *Phys. Rev. D* **3**, 825–839.
- Weinzierl, B., Petzold, A., Esselborn, M., Wirth, M., Rasp, K. and co-authors. 2008. Airborne measurements of dust layer properties, particle size distribution and mixing state of Saharan dust during SAMUM 2006. *Tellus* **61B**, doi: 10.1111/j.1600-0889.2008.00392.x.
- Wieland, D. J., Mishchenko, M. I., Macke, A. and Carlson, B. E. 1997. Improved t-matrix computations for large, nonabsorbing and weakly absorbing nonspherical particles and comparison with geometrical-optics approximation. *Appl. Opt.* **36**, 4305–4313.
- Yang, P. and Liou, K. N. 1996. Geometric-optics-integral-equation method for light scattering by nonspherical ice crystals. *Appl. Opt.* **35**, 6568–6584.
- Yang, P., Feng, Q., Hong, G., Kattawar, G., Wiscombe, W. and co-authors. 2007. Modeling of the scattering and radiative properties of nonspherical dust-like aerosols. *J. Aerosol Sci.* **38**, 995–1014.
- Yee, K. 1966. Numerical solution of initial boundary value problems involving Maxwell's equations in isotropic media. *IEEE Trans. Ant. Propag.* **14**, 302–307.
- Zakharova, N. T. and Mishchenko, M. I. 2000. Scattering properties of needlelike and platelike ice spheroids with moderate size parameters. *Appl. Opt.* **39**, 5052–5057.